J. Fluid Mech. (2005), *vol.* 545, *pp.* 245–269.
doi:10.1017/S0022112005006968 Printed in the United Kingdom

On the orientation of stiff fibres suspended in turbulent flow in a planar contraction

By MEHRAN PARSHEH[1], MATTHEW L. BROWN[2] AND CYRUS K. AIDUN[3]

[1]Institute of Paper Science and Technology, Georgia Institute of Technology Atlanta, GA 30332, USA

[2]School of Chemical and Biomolecular Engineering, Georgia Institute of Technology Atlanta, GA 30332, USA

[3]G.W. Woodruff School of Mechanical Engineering, Georgia Institute of Technology Atlanta, GA 30332, USA

(Received 28 June 2004 and in revised form 17 June 2005)

The influence of turbulence on the orientation state of a dilute density matched suspension of stiff fibres at high Reynolds number in a planar contraction is investigated. High-speed imaging and laser-Doppler velocimetry techniques are used to quantify fibre orientation distribution and turbulent characteristics. A nearly homogeneous isotropic grid-generated turbulent flow is introduced at the contraction inlet. Flow Reynolds number and inlet turbulent characteristics are varied in order to determine their effects on orientation distribution. The orientation anisotropy is shown to be accurately modelled by a Fokker–Planck type equation. Results show that rotational diffusion is highly influenced by inlet turbulent characteristics and decays exponentially with convergence ratio. Furthermore, the effect of turbulent energy production in the contraction is shown to be negligible. Also, the results show that the flow Reynolds number has negligible effect on the development of orientation anisotropy, and the influence of turbulence on fibre rotation is negligible for rotational Péclet number >10.

1. Introduction

Fibres suspended in flow undergo mean motion owing to the mean fluid velocity, random motion due to the fluctuating component of the fluid velocity and inertia-driven motion. In many industrial processes, the behaviour and orientation of fibres in a turbulent flow affects the transport, rheology and turbulent characteristics of suspensions. In the paper industry, mechanical properties of manufactured paper are known to be anisotropic owing to the anisotropic orientation of fibres induced by the flow kinematics while passing through a planar contraction with flat walls. The degree of fibre orientation anisotropy has a significant impact on the product quality. Defects, such as curl in papers resulting in paper jamming in copier machines and printers, are primarily due to fibre orientation anisotropy. Therefore, in addition to the fundamental importance of understanding the influence of turbulence and mean flow on fibre orientation, this problem is of practical interest in industrial processes.

In many industrial applications, the microscopic and macroscopic Reynolds numbers are large and thus the inertia of discrete and continuous phases cannot be neglected. When the particle Reynolds number is $O(1)$ or greater, finite fibre

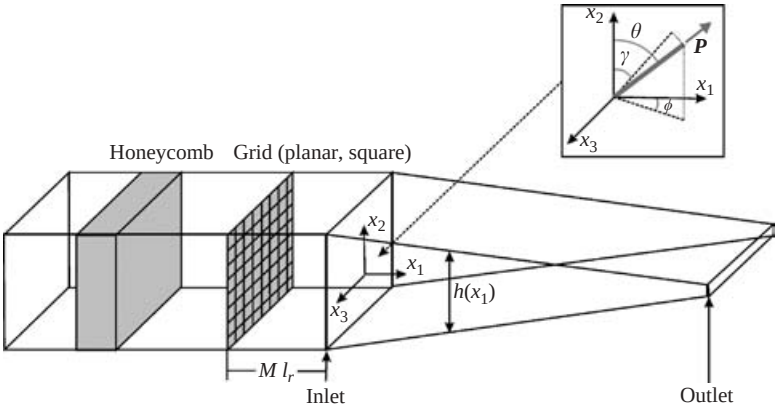

FIGURE 1. Schematic of the experimental set-up with coordinate system.

inertia affects the motion and the Stokes flow simplifications do not apply. In gas–particle suspensions where the flow is characterized by a large particle Stokes number and a relatively small fluid Reynolds number, the particle inertia is important and the fluid inertia is negligible. Thus, the fluid equation can be simplified to the linear Stokes equation while the complete Navier–Stokes equation should be solved for the flow adjacent to the particle surface (Koch & Hill 2001). The governing equations become more complex when the Reynolds number of both particle and the fluid are $O(1)$ or greater. Although there is no averaged equation of motion for these flows, computations based on direct numerical simulation (DNS) can accurately predict the behaviour of the interacting particles (Bunner & Tryggvason 1999).

The macroscopic Reynolds number is defined based on the local mean streamwise velocity in the contraction, U_1, and the contraction local height, h, given by (see figure 1)

$$Re = \frac{U_1 h}{\nu}, \tag{1}$$

where ν is the kinematic viscosity of fluid (water in this study). In this paper, we study the effect of turbulence on orientation distribution of fibres suspended in water in a planar contraction at high-flow Reynolds number. The experiments are conducted at $Re = 85 \times 10^3$ to 170×10^3.

In various investigations (e.g. Cox 1970; Harris & Pittman 1976; Olson & Kerekes 1998; Olson 2001) the microscopic Reynolds number is based on fibre length. However, Bernstein & Shapiro (1994) used the fibre diameter as the length scale and concluded that since the microscopic Reynolds number based on this length scale is small, the effect of fibre inertia in their experiments is negligible. Since these investigations do not include the motion of fibres with large fluid Reynolds number, it is not clear which length scale can effectively describe the effect of fibre inertia. Analogous to these studies, we define the microscopic Reynolds number based on the streamwise mean local rate of strain, $\partial U_1/\partial x_1$, and fibre half-length, L, given by

$$Re_f = \frac{(\partial U_1/\partial x_1)L^2}{\nu}. \tag{2}$$

In the experiments presented in this study, the magnitude of Re and Re_f are $O(10^5)$ and $O(10^2)$ at the contraction outlet, respectively. Because of high Re_f, the fibre inertia can be important. However, considering fibre diameter as the length scale,

Re_f will be small enough to imply no effect of fibre inertia. The force balance in the streamwise direction shows that fibre velocity induced by the drag force is dependent on the fibre diameter, d_f, and the liquid and fibre density ratio. Thus, the relative velocity of fibre and the carrier liquid is a function of fibre diameter only, if the ratio of fibre to liquid density is approximately equal to one. For the fibre dimensions and suspension properties used in this study, the slip velocity is very small. Assuming the fibre diameter is the characteristic length scale, the time scale of the fibre, τ_f, is given by

$$\tau_f = \frac{d_f(\partial U_1/\partial x_1)}{U_1(\partial U_1/\partial x_1)} = \frac{d_f}{U_1}. \tag{3}$$

For $Re = 85 \times 10^3$ and fibre diameter 57 μm, the fibre inertial time response varies from $\tau_f = 0.14$ ms at $x_1 = 0$ to $\tau_f = 0.0125$ ms at the contraction outlet (see figure 1). The characteristic time scale, τ_a, due to acceleration of mean flow is given by

$$\tau_a = \left(\frac{\partial U_1}{\partial x_1}\right)^{-1}. \tag{4}$$

For the same flow Reynolds number, the time scale of the convective acceleration varies from $\tau_a = 2500$ ms at $x_1 = 0$ to $\tau_a = 2$ ms at the outlet. The acceleration Stokes number, St_a, defined as

$$St_a = \frac{\tau_f}{\tau_a}, \tag{5}$$

varies from 5.6×10^{-5} to 6.25×10^{-3}. When St_a is $O(1)$ or greater, fibre inertia becomes an important factor influencing the dynamics. Thus, it can be concluded that the effect of inertia is negligible if the Reynolds number based on the fibre diameter, and not length, is the appropriate parameter. This question will be addressed when the distribution of the measured orientation anisotropy is compared to the theories for inertialess fibres in suspension.

Considering the flow is turbulent, in order to study the dynamics of fibre motion inside the contraction, it is necessary first to understand development of single-phase turbulent flow in this geometry. Applying the Kelvin circulation theorem to predict the intensity of turbulent vortices in an axisymmetric contraction, it can be shown that the streamwise component of turbulence decays through the contraction, whereas the transverse component grows (Prandtl 1933). The limitation of this Lagrangian approach is that the model does not account for mutual interaction of continuum vortices. A new model was put forth by Taylor (1935) using Cauchy's equations and assuming conservation of circulation. Taylor's model predicts a slower rate of decay for the fluctuating component of turbulence in the streamwise direction, and a slower rate of amplification for the transverse fluctuating component. Based on comparison with experimental data, the model developed by Batchelor & Proudman (1954) and Ribner & Tucker (1953) more accurately predicts the development of turbulent kinetic energy as a function of the total rate of strain on a fluid element. This model is only valid for rapid distortions, where the time scale of the flow is much smaller than the time scale of eddy interaction. Therefore, the fluid viscosity and the interaction between eddies are ignored. Another limitation of the rapid distortion theory (RDT) is that the characteristic turbulent scale must be much smaller than the spatial scales of the mean flow.

Experimental studies of the development of turbulent quantities in an axisymmetric contraction show that Prandtl's theory only holds for contraction ratios, $C < 4$. The contraction ratio, C, is defined as the ratio of the local mean velocity to the inlet mean

velocity. According to Uberoi (1956), the measured streamwise component becomes significantly higher than predicted at $C > 4$. This is attributed to the transfer of energy between longitudinal and transverse velocity fluctuations. Goldstein & Durbin (1980) show that the amplification of the streamwise Reynolds stress component after $C = 4$ is significantly reduced when the spatial scale of the turbulence increases. Another finding of this work is that the interaction between the turbulence and the mean flow increases with decreasing wavenumber. Tsuge (1984) found that small eddies decay through the contraction, in agreement with Batchelor & Proudman (1954). However, large eddies are amplified owing to the stretching of vortices.

Hussain & Ramjee (1976) investigated the effect of the shape of the contractions on core flow. They measured velocity field in four different axisymmetric contractions with identical total acceleration. They concluded that the acceleration is the primary parameter. Many other investigators have studied different aspects of flow through axisymmetric contractions. Townsend (1954) and Tucker & Reynolds (1968) investigated the effect of contraction on the core turbulent flow with constant rate of strain. Townsend found that after a certain degree of strain, an equilibrium structure of turbulence is established. The mechanisms that transfer energy between the different components are then so effective that further strain produces only a small alteration in the structure. However, Tucker & Reynolds argue that the flow never reaches an equilibrium structure.

Existing analytical models used to predict turbulence in contractions are shown to be inaccurate for large C. Several numerical simulations of turbulent plane strain flow have been performed to investigate the structure of homogeneous turbulence subject to irrotational strain (e.g. Kwak, Reynolds & Ferziger 1975; Lee & Reynolds 1985). However, these studies are restricted to low Re flow with constant rate of strain.

The focus of this study is on the dynamics and orientation of dilute fibre suspensions in turbulent flow. In such dilute systems, each fibre can rotate freely without interacting with other fibres. A non-interacting suspension is characterized by $nL^3 \ll 1$ or $\phi_c \ll 1$ for large-aspect-ratio fibres, where n is the number density of fibres, L is the fibre half-length, and ϕ_c is the fibre volume fraction. According to Doi & Edwards (1978), the transition from an infinitely dilute non-interacting suspension to a semi-dilute interacting suspension occurs at $\phi_c a_p^2 = O(1)$, where a_p is the fibre aspect ratio (the ratio of fibre length to diameter).

We can approximate the shape of a fibre as an ellipsoid with a large aspect ratio. The dynamics and orientation of an inertialess ellipsoid in the dilute regime in laminar flow is given by Jeffery's relation (1922) and its generalization to any axisymmetric particle is given by Brenner (1974). The preferential alignment of fibres in one direction changes the suspension's bulk properties and makes the transport tensors anisotropic. An expression for the contribution of fibres to the bulk average deviatoric stress, in terms of rate of strain tensor and orientation vector, is derived by Batchelor (1971). In non-interacting dilute suspension of fibres, this contribution is given by

$$\mu_f \approx \tfrac{4}{3}\pi \frac{nL^3}{\ln(a_p)}\mu, \tag{6}$$

where μ is the dynamic viscosity of the carrier fluid.

A limited number of studies has focused on the motion of rigid fibres in turbulent flow. In turbulent flow, the dispersion of individual fibres is altered owing to the presence of velocity fluctuations. Krushkal & Gallily (1988) studied the development

of orientation distribution of non-spherical aerosol particles in a turbulent shear flow. They concluded that particles become randomly oriented in the presence of strong turbulence. However, for flow with mean velocity gradients, the orientation distribution function is anisotropic if the turbulent intensity is not large enough to randomize the particles. Bernstein & Shapiro (1994) investigated the orientation of glass fibres in laminar and turbulent pipe flow. They found that at low-Reynolds-number laminar flow, the fibres are randomly distributed near the pipe centre. As the Reynolds number increases within the laminar regime, the fibres become more oriented in the streamwise direction. At high-Reynolds-number turbulent flow, the randomizing effect of the turbulence leads to an almost random orientation.

Orientation anisotropy of fibres in a planar contraction has been studied by various investigators. Harris & Pittman (1976) studied a dilute suspension of fibres in a planar contraction with $Re = 1000$. Owing to low microscopic Reynolds number, the effect of fibre inertia was negligible. The fibre orientation anisotropy was found to vary with C and to be independent of Re, ν, a_p and contraction half-angle, β. However, in most fibre suspension flows of interest, the influence of fibre inertia and turbulence on orientation cannot be neglected. Ullmar & Norman (1997) and Ullmar (1998) measured the orientation anisotropy of nylon fibres in the (x_1, x_3)-plane (see figure 1) in a straight channel downstream of the contraction outlet. The flow inlet to the contraction consists of a series of turbulence-generating step expansion tubes positioned immediately upstream of the inlet. In these studies, the influence of flow Reynolds number, contraction ratio and fibre concentration on the orientation anisotropy is investigated. They concluded that the orientation anisotropy is strongly dependent on the contraction ratio and almost independent of the fluid Reynolds number. However, the turbulent fluctuations in these studies were not measured; therefore, they could not relate the orientation anisotropy to the turbulent flow characteristics. It should be noted that in their studies, the measured orientation distribution is an average over the entire height of a straight channel attached to the downstream of the contraction outlet. It is known that the turbulent properties change in the straight channel and thus the measured orientation distribution would be different from that at the outlet of the contraction (see e.g. Harris & Pittman 1976).

Analogous to suspension flows with Brownian motion and fibre–fibre interaction, the effects of turbulence on orientation anisotropy have been modelled by a rotational diffusion coefficient tensor (e.g. Krushkal & Gallily 1988; Olson & Kerekes 1998; Olson *et al.* 2004). Olson & Kerekes expressed the turbulence-induced rotational diffusion coefficient in an isotropic turbulent flow as a function of turbulent integral time and length scales, turbulent intensity and fibre length. They found that by increasing the ratio of the fibre length to the Lagrangian integral length scale, the diffusion coefficient decreases. Olson *et al.* (2004) numerically solved the Fokker–Planck equation governing the orientation distribution of fibres at the centreline of a planar contraction. They state that the rotational diffusion coefficient, D_r, is constant throughout the contraction and $D_r = 2\,\mathrm{s}^{-1}$ gives the best agreement with the experimental studies of Ullmar (1998) and Zhang (2001). A quantitative comparison requires orientation measurements at the contraction centreline (as done in this study) where the equations are derived. The measurement of fibre orientation distribution at a straight channel downstream of the contraction outlet represents an average of all fibres and is, therefore, inconsistent with the governing equations for the centreline.

The objective of our study is to determine the effect of turbulence on the orientation distribution function of fibres in a planar contraction. To understand the impact of

turbulence on orientation anisotropy requires measurement of orientation at different streamwise positions in the contraction with clearly defined turbulent conditions at the inlet and knowledge of turbulent flow variations along the contraction. Therefore, the experiment is designed so that the fibre–fibre interactions and the effect of the fibres on the flow rheology become negligible. Nearly homogeneous isotropic grid turbulent flow is introduced at the channel inlet and its variation in the contraction is measured. Since the influence of turbulence on orientation anisotropy can be expressed by an orientational diffusion coefficient, in this paper we also examine the factors affecting this coefficient. In order to distinguish the effect of inlet flow characteristics from the produced turbulence in the contraction, the turbulent intensity at the channel inlet is varied by adjusting the position of the grid relative to the inlet. Since the turbulent intensity decays in the contraction and eventually the flow becomes nearly laminar, this approach provides an opportunity to examine the effect of turbulence on the dynamics of fibre orientation. In order to obtain reliable average data, the motion of a large population of fibres is quantified and the development of the orientation distribution function at different downstream positions in the contraction is examined.

2. Theory

In this section, we discuss the theoretical background for the dynamics of fibre orientation in laminar flow, followed by application of existing fibre orientation models in turbulent flow.

In this study, the fibres can be assumed to be rigid since the viscous drag force is insufficient to deform the fibres. To verify this point, let us consider the dimensionless parameter $Z \equiv [2\pi\mu(\partial U_1/\partial x_1)(2L)^4)/(B\ln(2a_p)]$, which represents the ratio of viscous drag force to the elastic recovery force of the fibre in dilute suspensions (Becker & Shelley 2001). In this equation, B is the effective bending rigidity which is equal to the product of the Young's modulus and the second moment of area, $I = \pi d_f^4/64$. For a typical rayon fibre with 60 μm diameter and 3.2 mm length and a Young's modulus 2 GPa, the maximum value of Z is $O(10^{-2})$ at the contraction outlet. This shows that hydrodynamic stresses are insufficient to deform the rayon fibres.

Assuming a fibre can be approximated by a large-aspect-ratio ellipsoid, we note that the change in unit orientation vector, p_i, for a single ellipsoidal particle (Jeffery 1922) is given by

$$\frac{\partial p_i}{\partial t} = \Omega_{ij} p_i + \lambda(E_{ij} p_j - E_{kl} p_k p_l p_i), \tag{7}$$

where t denotes time, and the antisymmetric part, Ω_{ij}, and symmetric part, E_{ij}, of the velocity gradient tensor are given by

$$\Omega_{ij} = \frac{1}{2}\left(\frac{\partial U_i}{\partial x_j} - \frac{\partial U_j}{\partial x_i}\right), \tag{8}$$

$$E_{ij} = \frac{1}{2}\left(\frac{\partial U_i}{\partial x_j} + \frac{\partial U_j}{\partial x_i}\right), \tag{9}$$

respectively, and λ is a function of aspect ratio of the ellipsoid, defined as

$$\lambda = \frac{a_p^2 - 1}{a_p^2 + 1}. \tag{10}$$

The instantaneous velocity component of the fluid are defined as $u_i = (U_1 + u_1', U_2 + u_2', U_3 + u_3')$. Considering the contraction shown in figure 1 with the origin of the

coordinate system located at contraction inlet and the streamwise direction denoted by x_1, the mean velocity gradient tensor for the core flow is given by

$$\frac{\partial U_i}{\partial x_j} = \begin{pmatrix} \dfrac{\partial U_1}{\partial x_1} & \dfrac{\partial U_1}{\partial x_2} \cong 0 & \dfrac{\partial U_1}{\partial x_3} \cong 0 \\ \dfrac{\partial U_2}{\partial x_1} & -\dfrac{\partial U_1}{\partial x_1} & 0 \\ 0 & 0 & 0 \end{pmatrix}. \tag{11}$$

If the effect of the sidewalls is negligible, the mean velocity in the x_3-direction, U_3, is zero. Far downstream of the grid, the streamwise mean velocity profile, U_1, along the x_2- and x_3-directions are uniform. In the contraction, the mean velocity profile remains uniform except at the boundary-layer region. Thus, $\partial U_1/\partial x_2$ and $\partial U_1/\partial x_3$ are approximately zero in the core flow. It is expected that the streamwise rate of strain, $\partial U_1/\partial x_1$, is the dominant term influencing fibre orientation in the contraction. The only non-zero component of the mean vorticity vector, which is responsible for production of turbulence in a contraction, is given by

$$\omega_3 = \frac{\partial U_2}{\partial x_1}. \tag{12}$$

However, this term is zero at the contraction centreline because of symmetry.

When there are many fibres suspended in the flow, the most complete description of the orientation state is through the probability distribution function of the fibre orientation, $\psi(\boldsymbol{p}, t)$ defined by

$$\oint \psi(\boldsymbol{p}, t)\, \mathrm{d}\boldsymbol{p} = 1, \tag{13}$$

where $\boldsymbol{p}$ is defined as the unit orientation vector along the longitudinal axis of the fibre (Dinh & Armstrong 1984). The planar distribution function for fibres aligned along the (x_1, x_3)-plane (i.e. $\theta = 90^\circ$), ψ^p is given by

$$\int_0^\pi \psi^p(\phi, t)\, \mathrm{d}\phi = 1. \tag{14}$$

Based on conservation principles in $\boldsymbol{p}$ space, the distribution function must satisfy the continuity equation given by

$$\frac{\mathrm{D}\psi}{\mathrm{D}t} + \nabla \cdot (\dot{\boldsymbol{p}}\psi) = 0, \tag{15}$$

where ∇ is the gradient operator in orientation space (i.e. the gradient operator of the surface of a unit sphere). The orientation distribution function provides the most general description of the orientation state of fibres. However, it is not possible to quantify directly the differences between two different distribution functions. We require a method to accurately represent ψ while readily quantifying the downstream development of orientation of fibres by a numerical index. Advani & Tucker (1987) show that even-order tensors give a concise description of ψ. The general fourth-order orientation tensor is given by

$$a_{ijkl} = \oint p_i p_j p_k p_l \psi(\boldsymbol{p})\, \mathrm{d}\boldsymbol{p}. \tag{16}$$

The fourth-order planar orientation tensor in the (x_1, x_3)-plane is defined as

$$a^p_{ijkl} = \int_0^\pi p_i p_j p_k p_l \psi^p(\phi)\, \mathrm{d}\phi. \tag{17}$$

These symmetric tensors are functions of time and position and represent moments of the orientation distribution function. The diagonal components of the orientation tensor show the degree of the alignment and the off-diagonal terms represent the skewness. Orientation distribution functions can be accurately reproduced given the orientation tensor components. Similar to other investigations (e.g. Advani & Tucker 1990; Azaiez, Guenette & Ait-Kadi 1997; Chiba, Yasuda & Nakamura 2001), in this study the single component of the fourth-order planar orientation tensor, a^p_{1111}, is used as a parameter to show the development of the orientation distribution function. It is important to note that a^p_{1111} only serves as an effective parameter to quantify planar orientation state. From this point on, the superscript 'p' in a^p_{1111} is dropped for convenience.

Analogous to suspension flows with Brownian motion, and semi-dilute suspensions with fibre–fibre interactions, the time rate of change of the orientation distribution function $\psi(\boldsymbol{p}, t)$ in turbulent flow is modelled by a Fokker–Planck type equation (see Advani & Tucker 1987; Doi & Edwards 1988; Krushkal & Gallily 1988; Koch 1995; Olson & Kerekes 1998), given by

$$\frac{\mathrm{D}\psi}{\mathrm{D}t} = D_r \nabla^2 \psi - \nabla \cdot (\dot{\boldsymbol{p}} \psi), \tag{18}$$

where D_r is the rotational diffusion coefficient which is assumed to be isotropic. In this equation, the translational diffusion is neglected because the fibre concentration in the suspension flow is assumed to be uniform. Depending on the flow conditions, the diffusion term on the right-hand side of (18) represents the randomization effect due to either the Brownian motion (Doi & Edwards 1988), hydrodynamic fibre–fibre interaction (Koch 1995) or the turbulent eddies (Olson & Kerekes 1998). In the present study, this model implies that fibre orientation development is the interplay between the arranging effect of the velocity gradient field and the randomizing effect of the turbulent eddies.

The rotational diffusion coefficient, D_r, has been modelled by several investigators. Krushkal & Gallily (1988) used a relationship based on Kolmogoroff's local isotropy hypothesis for small eddies, and from dimensional analysis derived the expression,

$$D_r \approx \left(\frac{\varepsilon}{\nu}\right)^{1/2}, \tag{19}$$

where ε is the dissipation rate of turbulent energy per unit mass, given by

$$\varepsilon = \nu \sum_{i,j} \overline{\left(\frac{\partial u_i'}{\partial x_j}\right)^2}, \tag{20}$$

(Hinze 1975). Olson (2001) proposed a modification to the rotational diffusion coefficient of Krushkal & Gallily, given by

$$D_r \approx 0.7 \left(\frac{4\varepsilon}{15\nu}\right)^{1/2}. \tag{21}$$

Olson & Kerekes (1998) employed a statistical analysis of the equation of motion for a single fibre moving in homogeneous isotropic turbulent flow to derive relations for turbulence-induced rotational and translational diffusion coefficients. They suggest that for long fibres, where the Lagrangian particle velocity correlation is the same as the fluid's Eulerian velocity correlation (Olson & Kerekes 1998), the rotational diffusion coefficient is given by

$$D_r = 24\,\overline{u_1'^2}\frac{\tau}{(2L)^2}\frac{\Lambda}{2L}\left(\operatorname{erf}\left(\frac{\pi^{1/2}(2L)}{2\Lambda}\right)+\frac{16}{\pi^2}\left(\frac{\Lambda}{2L}\right)^3(1-\exp(-\pi(2L)^2/4\Lambda^2))+\frac{2}{\pi}\frac{\Lambda}{2L}(\exp(-\pi(2L)^2/4\Lambda^2)-3)\right). \quad (22)$$

This model implies that for long fibres, D_r is a function of the fluid Eulerian integral time scale, τ, Eulerian integral length scale, Λ, and streamwise component of fluctuating velocity.

A primary objective in this study is to investigate the impact of turbulence on fibre orientation. However, the turbulent intensity varies significantly downstream from the inlet as the contraction ratio increases. To investigate the variation in turbulent intensity, let us consider the general energy production term in the Reynolds stress transport equation, given by

$$P_{ij} = -\overline{u_i'u_l'}\frac{\partial U_j}{\partial x_l} - \overline{u_j'u_l'}\frac{\partial U_i}{\partial x_l}. \quad (23)$$

Considering the velocity gradient tensor of the flow in the planar contraction, given by (11), the normal components of the energy production for turbulent flow at the contraction centreline simplify to

$$P_{11} = -2\overline{u_1'^2}\frac{\partial U_1}{\partial x_1}, \quad (24)$$

$$P_{22} = 2\overline{u_2'^2}\frac{\partial U_1}{\partial x_1}, \quad (25)$$

$$P_{33} = 0, \quad (26)$$

and the turbulent kinetic energy production at the contraction centreline is given by

$$K_p = \left(\overline{u_2'^2} - \overline{u_1'^2}\right)\frac{\partial U_1}{\partial x_1}. \quad (27)$$

Considering a homogeneous, isotropic turbulent flow at the inlet, equations (24) and (25) imply that the fluctuating velocity component in the x_1-direction is likely to decrease, and in the x_2-direction to increase, because of the negative and positive signs of the production terms in these directions, respectively. This is in agreement with Prandtl's theory (1933). In addition, production of turbulent kinetic energy is expected to be almost zero, since in equation (27), $\overline{u_1'^2}$ and $\overline{u_2'^2}$ are almost equal in magnitude. This implies that for an isotropic turbulent flow at the inlet, the turbulent kinetic energy is expected to decrease owing to negligible production and finite viscous dissipation. Further downstream, where the flow becomes significantly anisotropic, the production term becomes larger than the rate of dissipation. We show below, in the analysis and results section, that this relation is consistent with the measurement of turbulent fluctuating components as a function of contraction ratio, C, from the inlet to the outlet of the contraction.

In the following sections, we present measurements of turbulent flow field and fibre orientation distribution and show the relative significance of mean velocity gradient and turbulent parameters on the evolution of fibre orientation distribution in the contraction.

3. Experimental set-up and data processing technique

The method used to quantify turbulence development and fibre motion in the contraction is based on laser-Doppler velocimetry (LDV) and high-speed imaging. Velocity field measurements of single-phase flow and visualization of dilute fibre suspension flow were carried out in a small closed water loop. The test section is constructed of 12 mm thick Plexiglas to allow for visual access. Flow first passes through a hexagonal flow straightener installed in a constant cross-section channel upstream of the contraction. The flow straightener has an open width of 10 mm and a closed width of 0.4 mm. Free-stream turbulence is then generated by a monoplane square grid with rectangular bars. The mesh size, M, and bar width of the grid are 9.5 mm, and 3.2 mm, respectively, resulting in a solidity of 0.56 (the solidity is defined as the grid geometric blockage area divided by the total area). The turbulent intensity at the contraction inlet is changed by repositioning the grid relative to the contraction inlet. This distance is normalized by mesh size, M, and is denoted by l_r hereinafter. In order to achieve homogeneous isotropic turbulence at the contraction inlet, the grid was located at least 20 mesh sizes upstream of the contraction inlet. The contraction is 550 mm in length, 155 mm in width and the inlet height is 179.2 mm. In most of the experiments presented, the outlet height is 16 mm, giving the contraction half-angle, $\beta = 8.4^\circ$, and maximum contraction ratio of 11.2. The contraction ratio is defined as

$$C = \frac{U_1}{U_{1,0}}, \tag{28}$$

where U_1 and $U_{1,0}$ are the local streamwise mean velocity and the streamwise mean inlet velocity, respectively. Contractions with different maximum contraction ratio, C_{max}, are obtained by changing the outlet height. The estimated velocity components $U_{1,p}$ and $U_{2,p}$ based on potential flow are given by

$$U_{1,p} = \frac{\nu Re}{h_0 - 2x_1 \tan\beta}, \tag{29a}$$

$$U_{2,p} = -\frac{2\nu \tan\beta Re}{(h_0 - 2x_1 \tan\beta)^2} x_2, \tag{29b}$$

where h_0 denotes the contraction inlet height. The flow Reynolds number, Re, is constant throughout the contraction. The development of the streamwise mean rate of strain in the contraction with the above dimensions is shown in figure 2, where $(\partial U_1/\partial x_1)_0$ denotes the velocity gradient at the inlet.

A TSI two-component LDV system is used to measure the instantaneous velocity field of single-phase water flow inside the contraction. The light source is a 5 W argon-ion laser (Coherent, Innova 70), and the scattering particles are 0.3 μm alumina. The elliptical measurement volume at the beam intersection is 0.1 mm in diameter and 4 mm in length. The optical head is traversed automatically using a three-dimensional linear traversing system with ± 0.01 mm accuracy. The maximum sampling rate of instantaneous velocity varies from 500 to 1500 samples s^{-1}. For consistency, measurements are sampled at a constant rate of 500 samples s^{-1} for a period of

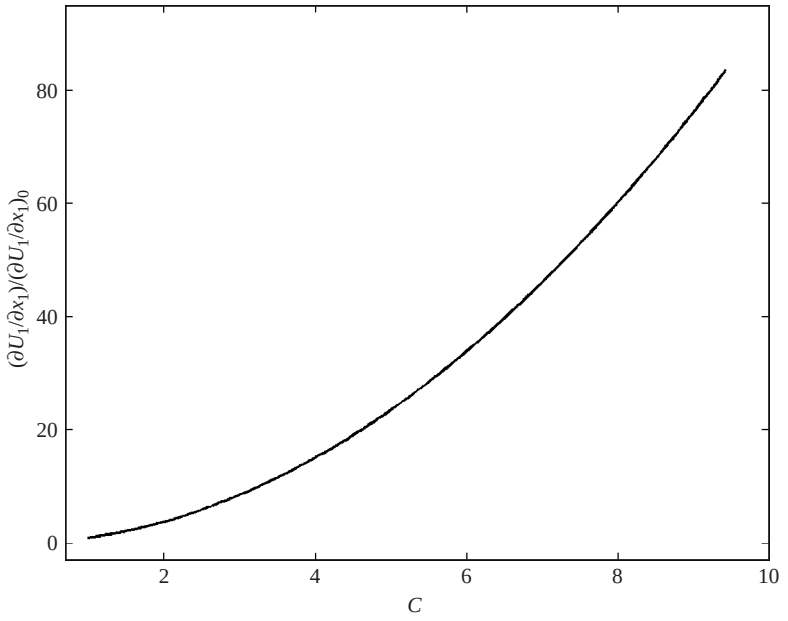

FIGURE 2. Normalized development of streamwise rate of strain along the converging channel's centreline.

90 s. In these experiments, Re is varied between 85×10^3 and 170×10^3, with exit velocity varying from 4.9 m s^{-1} to 9.8 m s^{-1}.

3.1. *Visualization and image processing technique*

An infinite dilute suspension of stiff opaque rayon fibres was visualized. The fibres are nominally 3.2 mm in length, 57 μm in diameter, with a specific gravity of 1.14. The suspension's nL^3-value is 0.0053, which suggests fibre–fibre interactions and the effects of fibres on flow rheology are negligible (see equation (6)). The fibres were dried by putting them for at least 24 h in an oven at temperature 105 °C.

The suspended fibres were visualized in the (x_1, x_3)-plane using a laser sheet and high-speed camera. A pulsed infra-red laser (Oxford model HSI1000) with pulse duration of 15 μs was synchronized with a V5 Phantom high-speed camera. A lens was used to project a 3.2 mm thick, 100 mm wide rectangular laser sheet into the contraction. The laser head was translated linearly in the x_2-direction with resolution ± 0.01 mm. The camera was translated linearly in the x_1-, x_2- and x_3-directions.

Images were taken at the centreplane of the contraction, defined as the (x_1, x_3)-plane located within $x_2 = \pm 1.6$ mm. Images have dimension of 9.6 mm in the x_1-direction and 14.5 mm in the x_3-direction with 342×512 pixel resolution. A total of 8190 image files are analysed at each position. The orientation distribution state is evaluated from a succession of approximately 4000 randomly imaged fibres at each position along the centreplane.

A complete software suite for analysing these images was developed. This software inverts the raw image, scans the frame, and identifies each fibre in the image. The few curved fibres encountered in the images were not considered in the orientation measurements. Since there is no fibre–fibre interaction, only the straight fibres are considered without biasing the resulting fibre orientation distribution function. Since all fibres are not perfectly straight, as shown in figure 3(a), to be very accurate we

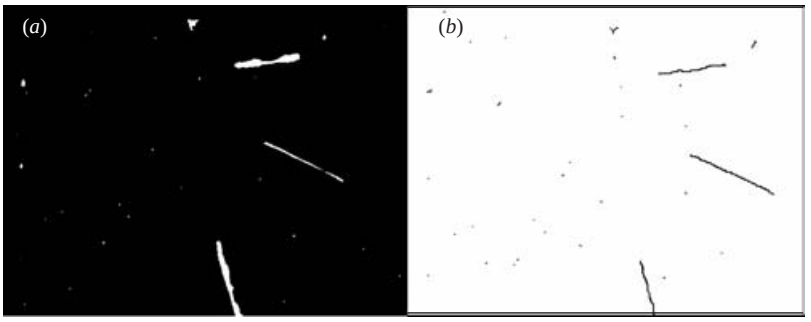

FIGURE 3. (*a*) Sample of raw images obtained from the visualization. (*b*) Image after inversion, background removal, binarization and skeletonization. The flow direction is from bottom to top.

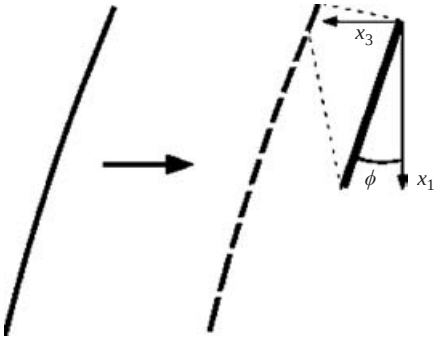

FIGURE 4. The schematic of the division of each fibre into segments and fitting lines by the least-squares technique.

divide each fibre into a number of segments, as shown in figure 4. Straight lines are fitted to each segment, and the angle distribution of the segments is averaged and used to determine the fibre orientation distribution. However, we find that the deviation of fibre shape from a straight line is so small that assuming the equation for a straight fibre provides us with an accurate prediction of orientation.

The following is a more detailed explanation of the data-processing procedure mentioned above. First, the background of each image is found by averaging 21 neighbouring frames. The background is then subtracted from the original images. This serves to eliminate the effect of lighting gradients as well as removing dirt and other artefacts. As a result, fibres are isolated on a clear background. Next, the images are binarized, which simplifies the subsequent orientation analysis. Once the images are properly conditioned, the position and orientation of each observed fibre is evaluated. Each binarized image of a fibre is eroded, using a skeletonizing algorithm, to single-pixel-width segments. This is accomplished by loading, in turn, each of the binarized frame images.

Each skeletonized fibre in the frame is then scanned to locate and eliminate each pixel that represents the intersection of two fibres. Each fibre of less than 0.64 mm in length is discarded as being a non-fibre image artefact. Data files are then written to document the position of each fibre in the frame. This process is repeated for every frame in the sequence. Figure 3 shows the raw image and the resulting processed image.

The orientation angle, ϕ, of each fibre is quantified once the images are properly conditioned and the position of each observed fibre has been evaluated. This is done

by starting from the head of the fibre to divide them into segments of 23 pixels (0.64 mm) long. Once the remaining part of the fibre dimension is smaller than 46 pixels, the division of the fibre is stopped and the remaining part is considered as a segment. Then, a line is fitted to each segment by the least-squares method. The orientation angles of measured fibres are arranged in bins of 3° increments to evaluate the orientation distribution function. Finally, the obtained orientation distribution function is normalized and plotted versus the bin centres.

In these measurements, the streamwise length of images is chosen to be three times the fibre length. The contraction ratio varies slightly along this length and therefore we use the effective contraction ratio which is defined as

$$C_e = \frac{1}{\Delta x_1} \int_{x_{1,1}}^{x_{1,2}} C(x_1)\, \mathrm{d}x_1,$$

where $\Delta x_1 = 9.6$ mm, and $x_{1,1}$ and $x_{1,2}$ are the upstream and downstream edge positions of the image, respectively. The straight channel upstream of the contraction inlet and the contraction are joined by a set of opaque flanges 30 mm in length. Owing to the presence of these flanges and the finite length of the images, the first position downstream of the contraction inlet is $C_e = 1.1$. From this point on the subscript 'e' is dropped for convenience.

4. Analysis and results

In this section, we present measurements of fibre orientation as well as the LDV measurements of the flow field. Before considering the effect of turbulence on fibre orientation, we must first characterize the development of the turbulent flow in the contraction. In the following paragraphs, we present results from the LDV measurements of the turbulent velocity fluctuations.

4.1. *Turbulence in planar contractions*

A nearly homogeneous, isotropic grid turbulent flow is introduced at the contraction inlet. At this position, the variations between the r.m.s.-velocity components are within $\pm 5\,\%$ outside the boundary layer. It has been observed that the mean velocity components can be closely approximated with the velocity components based on a simple quasi-one-dimensional potential flow, provided by equation (29) and demonstrated in figure 5. This can be attributed to the presence of uniform streamwise velocity profiles (i.e. $\partial U_1/\partial x_2 \cong 0$ and $\partial U_1/\partial x_3 \cong 0$) at the core region of the contraction, low turbulent intensity components, and the presence of a thin relaminarized boundary layer along the walls (Parsheh 2001). The velocity components based on potential flow are used in the fibre orientation analysis throughout this paper.

The decay of turbulent intensity behind a uniform grid in a straight channel has been approximated by several investigators. One such model for flow in a straight channel is given by Roach (1987),

$$\frac{\sqrt{\overline{u_1'^2}}}{U_{1,0}} = c_o \left(\frac{l}{d}\right)^{-5/7}, \tag{30}$$

here, $U_{1,0}$ is the streamwise mean velocity in the straight channel upstream of the contraction inlet, l is the downstream position from the grid, d is the grid bar width and c_o is a constant based on grid geometry. However, the magnitude of the exponent varies in different investigations. For example, Groth & Johansson (1988) obtained -0.50 and Westin *et al.* (1994) obtained -0.62. If it is assumed that the

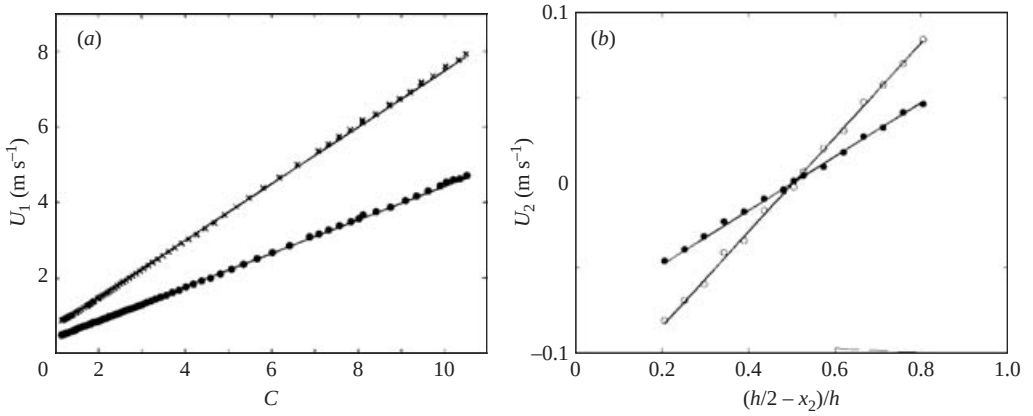

FIGURE 5. (*a*) Measured streamwise mean velocity along the contraction centreline, $Re = 85 \times 10^3$ (●) and $Re = 150 \times 10^3$ (○) compared to potential theory (—). (*b*) Measured mean velocity in the x_2-direction at $C = 1.1$ for $Re = 85 \times 10^3$ (●) and $Re = 150 \times 10^3$ (○) compared to pontential theory (—).

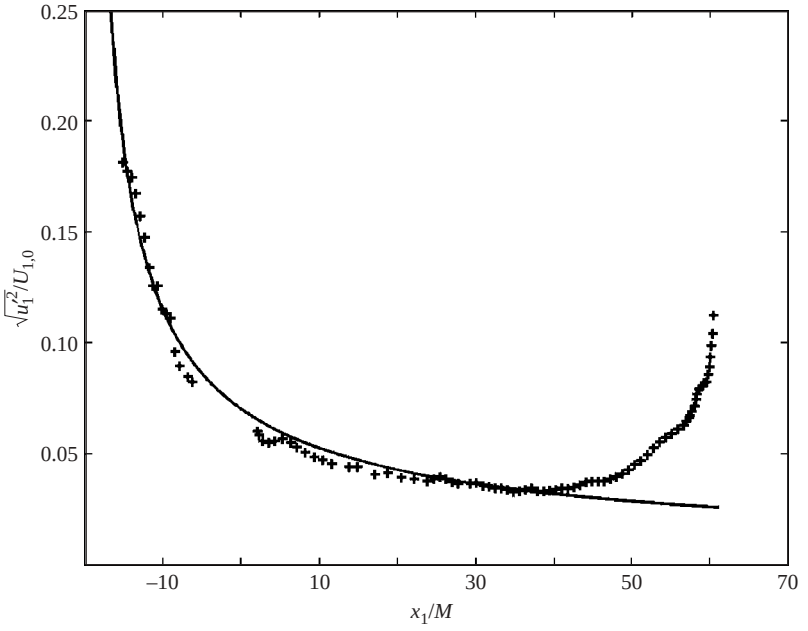

FIGURE 6. Normalized streamwise x_1-component of r.m.s.-velocity downstream of the monoplanar grid for case $Re = 85 \times 10^3$, $l_r = 20$ (+) compared to grid turbulence decay in a straight channel based on relation by Roach (1987) (—).

decaying turbulence can be predicted by the K-ε model, the exponent can be easily derived if the turbulent diffusion terms are neglected. This will give an exponent of -0.52 for the empirical coefficient $C'_{\varepsilon 2} = 1.8$. Figure 6 shows that, for the flow at the contraction centreline, this model agrees well with the measured data for up to $55M$ (55 mesh size) downstream of the grid, where $c_o = 1.13$ as specified by Roach (1987). The slight deviation between the measured results and results from equation (30) is most probably due to the dependence of c_o on Reynolds number when $Re > 10^4$. The

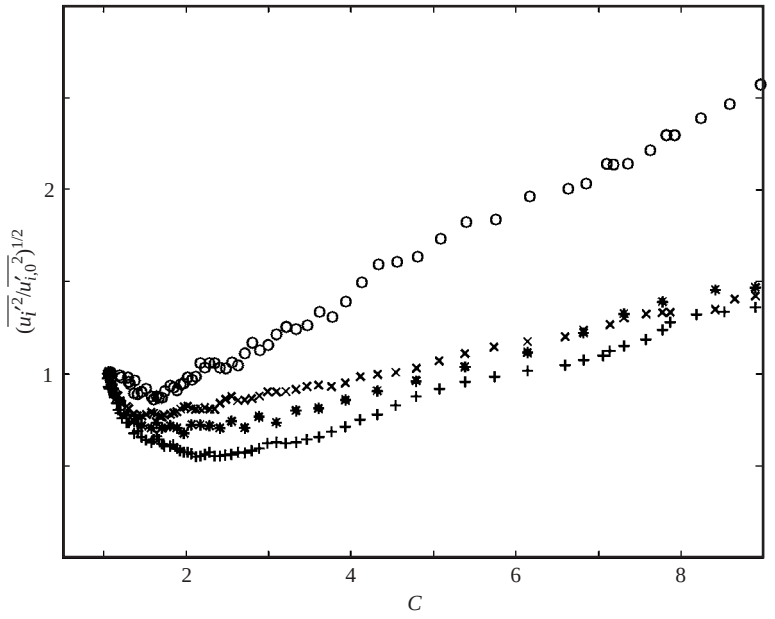

FIGURE 7. Normalized r.m.s.-velocity components along the channel centreline. The x_1-component (+), x_2-component (×), and x_3-component (*) at $Re = 85 \times 10^3$ and $l_r = 20$ are compared with the x_1-component at $l_r = 60$ (○).

agreement between decaying grid turbulent flow in constant cross-section channels and in the contraction at $C < 2$ suggests that the production of turbulence is very small in this region.

Figure 7 shows the normalized r.m.s.-velocity components at the contraction centreline in case $Re = 85 \times 10^3$ and $l_r = 20$ and the streamwise component in case $Re = 85 \times 10^3$ and $l_r = 60$. The development of the streamwise and cross-stream components when $l_r = 20$ are characterized by a minimum at $C = 2.1$ and $C = 1.7$, respectively. However, the minimum value of the streamwise component when $l_r = 60$ occurs at $C = 1.7$. This implies that the location of the minimum value is dependent on inlet turbulence conditions. The turbulence level in the x_1-direction should decrease, whereas in the x_2-direction should increase, since the production terms in the x_1- and x_2-directions have opposite signs. The total production of the kinetic energy is the sum of two terms with different signs. This implies that when an isotropic turbulent flow enters the contraction, the production of the turbulent kinetic energy would be zero immediately downstream of the inlet. This leads to decay of turbulent intensity because of dissipation. Further downstream, the turbulent kinetic energy increases because of anisotropy due to a higher Reynolds stress component in the x_2-direction than in the x_1-direction. This effect becomes amplified further downstream at the high contraction ratio region. The increase in the streamwise component of the turbulent kinetic energy is most probably because of inter-component distribution of energy.

The inlet value of the turbulent intensity nearly doubles when the grid position is moved downstream from $l_r = 60$ to $l_r = 20$. The streamwise turbulent intensity component along the centreline, $T_1 \equiv \sqrt{\overline{u_1'^2}}/U_1$, decreases monotonically downstream of the inlet to less than 1.5 % at the contraction outlet. Figure 8 shows this component for various cases with different flow Reynolds numbers ($Re = 85 \times 10^3$ and $Re = 170 \times$

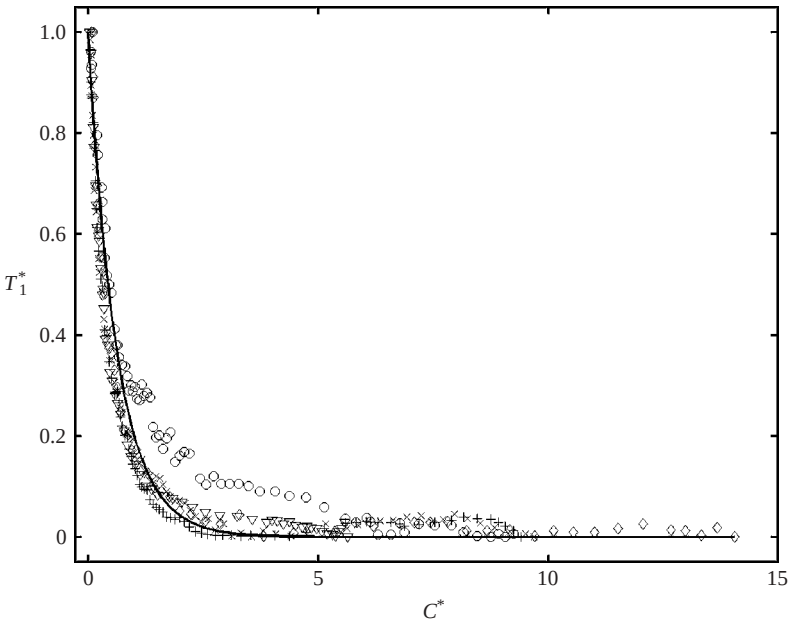

FIGURE 8. Streamwise component of turbulent intensity along the contraction centreline for $Re = 85 \times 10^3$, $l_r = 60$, and $\beta = 8.4°$ (○); $Re = 85 \times 10^3$, $l_r = 20$ and $\beta = 8.4°$ (+); $Re = 170 \times 10^3$, $l_r = 20$ and $\beta = 8.4°$ (×); $Re = 85 \times 10^3$, $l_r = 20$, and $\beta = 8.15°$ (∇); $Re = 85 \times 10^3$, $l_r = 20$, and $\beta = 8.8°$ (◇); and the exponential decaying curve fitted to data, ($e^{-1.6C^*}$). (—)

10^3), contraction half-angles and inlet turbulent conditions. In this figure, $T_1^* \equiv (T_1 - T_{1,e})/(T_{1,0} - T_{1,e})$ and $C^* \equiv C - 1$, where $T_{1,0}$ and $T_{1,e}$ are the values of T_1 at inlet and outlet, respectively. As shown in figure 8, these cases collapse around an exponentially decaying curve, $e^{-1.6C^*}$, where the coefficient -1.6 is based on the least-squares fit to the data. The exponentially decaying function presented above and $T_1^*(C^*)$ based on the power-law function of Roach (1987) almost overlap when $C < 2$. At $C > 2$, the exponential function is in better agreement to the experimental data. The deviation between these functions at $C > 2$ is probably due to the production of turbulent kinetic energy in the x_2-direction, given by equation (25), and the transfer of energy to the x_1-direction, as explained above.

4.2. *Dynamics of fibre orientation*

The orientation of a single fibre can be described by the angles (ϕ, θ) defined in figure 1. Goldsmith & Mason (1967) derived the general equations for the time rate of change of the orientation angles, ϕ and θ, in three-dimensional flows. The angular velocity components of large-aspect-ratio fibres, $\lambda \equiv 1$, for flow through planar contractions, from Goldsmith & Mason (1967) and also from (7) simplify to

$$\frac{\mathrm{d}\phi}{\mathrm{d}t} = -\frac{\partial U_1}{\partial x_1}\cos\phi\sin\phi, \tag{31}$$

$$\frac{\mathrm{d}\theta}{\mathrm{d}t} = -\frac{\partial U_2}{\partial x_1}\cos\phi\sin^2\theta + \frac{1}{4}\frac{\partial U_1}{\partial x_1}\cos(2\phi)\sin(2\theta) + \frac{3}{4}\frac{\partial U_1}{\partial x_1}\sin(2\theta). \tag{32}$$

The mean velocity gradients, computed at the centre of each fibre, are assumed to be constant along the fibre. The time rate of change of the angle, γ, between the x_2-axis

and the line of projection on the (x_1, x_2)-plane (see figure 1), is given by

$$\frac{\mathrm{d}\gamma}{\mathrm{d}t} = -\frac{\partial U_2}{\partial x_1}\sin^2\gamma + \frac{\partial U_1}{\partial x_1}\sin(2\gamma). \tag{33}$$

In addition to the trivial steady-state solution, $\gamma = 0$, the other stable steady-state solution is given when the fibres align with the streamlines.

The relationship between $\partial U_{1,p}/\partial x_1$ and $\partial U_{2,p}/\partial x_1$ from equation (29), is given by

$$\frac{\partial U_{2,p}}{\partial x_1} = -\frac{4\tan\beta}{h(x_1)}\frac{\partial U_{1,p}}{\partial x_1}x_2. \tag{34}$$

This equation shows that when $|x_2| \leqslant 0.3(h/2)$, $\partial U_{2,p}/\partial x_1$ is at least one order of magnitude smaller than $\partial U_{1,p}/\partial x_1$.

Equation (32) can be greatly simplified when applied to the centre symmetry plane; therefore we have focused the fibre orientation measurements in the region $|x_2| \leqslant L$, where L is the fibre half-length. The first term on the right-hand side of equation (32) is at least one order of magnitude smaller than the third term when

$$\frac{40\tan\beta}{h(x_1)}x_2 \leqslant \left|\frac{\cot\theta}{\cos\phi}\right|. \tag{35}$$

Considering a random orientation distribution, at least 90 % of fibres satisfy equation (35) at $x_1 = 0$ inside the region where $|x_2| \leqslant L$ (centreplane) for the contraction shown in figure 1. This assumption becomes even better when the flow develops downstream. Since only a small fraction of fibres do not satisfy the above criteria, their relative contribution to the overall orientation distribution is negligible. For the range of angles outlined above, equation (32) can be approximated by

$$\frac{\mathrm{d}\theta}{\mathrm{d}t} = \frac{1}{4}\left(\frac{\partial U_1}{\partial x_1}\right)\cos(2\phi)\sin(2\theta) + \frac{3}{4}\left(\frac{\partial U_1}{\partial x_1}\right)\sin(2\theta). \tag{36}$$

It is apparent from (31) and (36) that change of ϕ is independent of θ, however, the evolution of θ depends on ϕ through $\cos(2\phi)$. As these equations imply, fibres rotate toward the stable steady-state solution, $\phi = 0^\circ$ and $\theta = 90^\circ$, with angular velocity components $\mathrm{d}\theta/\mathrm{d}t \geqslant \mathrm{d}\phi/\mathrm{d}t$. However, the angular velocity components $\mathrm{d}\phi/\mathrm{d}t$ or $\mathrm{d}\theta/\mathrm{d}t$ are zero when the initial fibre angle, $\phi_o = 90^\circ$ or $\theta_o = 0^\circ$, respectively, since the acting moment on the fibre is zero. Solution of equation (31) is given by

$$\tan(\phi) = \tan(\phi_o)\mathrm{e}^{-\kappa}, \tag{37}$$

where

$$\kappa = \int_{x_{1,o}}^{x_1} \frac{1}{U_1}\left(\frac{\partial U_1}{\partial x_1}\right)\mathrm{d}x_1, \tag{38}$$

and the subscript 'o' denotes initial condition and κ is the total dimensionless acceleration imposed on the flow in the contraction from $x_{1,o}$ to x_1. This equation relates the planar evolution of the orientation angle of a single fibre, ϕ, to the flow acceleration in the contraction.

In this study, we have used the single component of the fourth-order planar orientational tensor, a_{1111}, as a parameter to quantify the orientation distribution function. To do this, the discrete form of equation (17) is used. The value of a_{1111} varies between 0 and 1.0 when all fibres are oriented in the x_3- and x_1-directions, respectively. For a perfectly random distribution of fibres, this value is 0.375.

Development of fibre orientation distribution along the contraction centreplane in turbulent flow, derived by substituting equation (31) into the planar form of equation (18), is given by

$$\frac{\partial \psi^p}{\partial x_1^*} = \frac{\partial^2 \psi^p}{\partial \phi^2} + Pe_r \frac{\partial}{\partial \phi}\left(\tfrac{1}{2}\psi^p \sin(2\phi)\right), \tag{39}$$

where $x_1^* = x_1/(U_1/D_r)$ is the dimensionless streamwise axis and the rotational Péclet number is defined as, $Pe_r \equiv (\partial U_1/\partial x_1)/D_r$. This equation shows that the relevant parameter, Pe_r, is the ratio of the mean velocity gradient to the rotational diffusion coefficient. Therefore, to predict the development of the fibre orientation distribution function we consider the variation of Pe_r with respect to the contraction ratio. In doing so, we have considered the dependence of D_r and $\partial U_1/\partial x_1$ on C. The variation of $\partial U_1/\partial x_1$ with C is clear. In the model by Olson & Kerekes (equation (22)), according to Taylor's hypothesis τ is given by Λ/U_1 and therefore, $\overline{u_1'^2}(\tau/(2L)^2)(\Lambda/2L)$ can be written as $(\sqrt{\overline{u_1'^2}}\Lambda^2 T_1)/(2L)^3$. This relation may be approximated by $\sqrt{\overline{u_1'^2}}T_1/2L$, since, as shown in the next section, in these experiments Λ is the same order of magnitude as L throughout the contraction. Consistent with Olson & Kerekes's model (1998), we consider that D_r varies in proportion to turbulent intensity in the contraction. Our measurements show that turbulent intensity decays exponentially with C, that is $e^{-1.6C^*}$, as discussed in the previous section, and shown in figure 8. At $C > 4$, turbulent intensity becomes very small, but finite owing to the small production of turbulent energy. However, in this region (i.e. $C > 4$) the effect of turbulence on fibre orientation becomes negligible where the effect of mean velocity gradient on fibre orientation becomes dominant. To represent effectively the competing roles of turbulence and mean velocity gradient on fibre orientation distribution in the contraction, we write the rotational Péclet number in the form,

$$Pe_r = \frac{2L}{T_{1,0}}\left(\frac{\mathrm{d}C}{\mathrm{d}x_1}\right) e^{0.95C}, \tag{40}$$

where the exponential term appears because of the exponential decay of turbulent intensity, and the coefficient of 0.95 is based on the least-squares fit to all the data from this study. In this analysis, the initial orientation distribution function is measured at $C = 1.1$ and the value of U_1 and $\partial U_1/\partial x_1$ are evaluated at the centre of the fibre. We show in figure 9 that this model accurately predicts all of the data within the range of parameters (Re, β, $T_{1,0}$) covered in this study. To do this, we calculate the parameter a_{1111} by solving equation (39). The results are normalized with the initial value ($a_{1111,o}$) measured at $C = 1.1$ and compared with the experimental data.

As shown in figure 9, the case considered by Olson *et al.* (2004) is different from the experiments in this study. This can be attributed to the fact that data by Ullmar (1998) are not obtained in the contraction. In addition, the inlet flow and turbulent characteristics in the experiments by Ullmar (1998) and Zhang (2001) are different from this study.

4.3. *Effect of turbulence on orientation*

The models proposed by Krushkal & Gallily (1988) and Olson & Kerekes (1998), given by equations (19) and (22), respectively, are evaluated from the measured turbulence characteristics in the contraction. In order to evaluate equation (22), the streamwise Eulerian integral time scale, τ, is evaluated from the autocorrelation of the streamwise instantaneous velocity signal. The integral length scale, Λ, is estimated

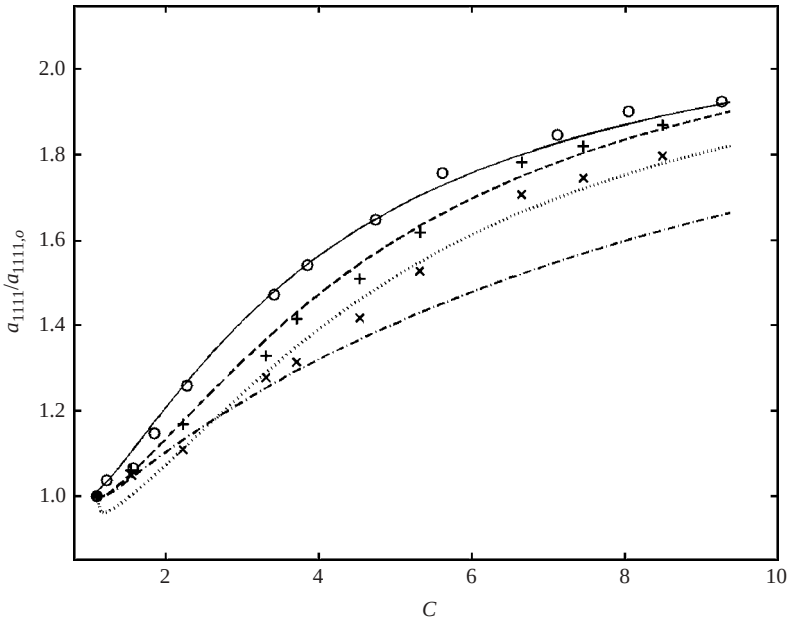

FIGURE 9. Comparison of measured (○) a_{1111} at $Re = 85 \times 10^3$ and $l_r = 60$ with current model (—) and Olson's model with $D_r = 2\ \mathrm{s}^{-1}$ (- - -); measured (+) at $Re = 85 \times 10^3$ and $l_r = 20$ with current model (- - -); measured (×) at $Re = 170 \times 10^3$ and $l_r = 20$ with current model (· · ·) using the measured distribution at $C = 1.1$ as the initial distribution function. All graphs are normalized by $a_{1111,o,}$ which is the measured value of a_{1111} at $C = 1.1$.

from the integral time scale based on Taylor's hypothesis. The Eulerian integral length scale varies from $4L$ at the inlet to $20L$ at $C = 8$, independent of the Reynolds number, where L denotes the fibre half-length. The downstream increase in the length scale is due to the dissipation of small eddies and stretching of turbulent eddies in the contraction. Furthermore, the integral time scale varies independently of the Reynolds number from $3.6L/U_{1,0}$ at the inlet to $6L/U_{1,0}$ at $C = 8$ with a minimum value of $1.6L/U_{1,0}$ at about $C = 2$, where $U_{1,0}$ denotes the streamwise mean velocity at the inlet. It is observed that at the region close to the contraction inlet, D_r based on the model given by equation (22) is of the same order of magnitude as the value obtained from equation (40). However, the values of D_r by equation (22) differ to results by equation (40), which may be explained by the fact that equation (22) is valid only in homogeneous isotropic flow and for long fibres. The accuracy of the rotational diffusion model given by equation (19) is evaluated using the measured streamwise velocity time signal to estimate ε. It is assumed that small-scale eddies are locally isotropic in the contraction. The value of D_r based on this model is two orders of magnitude larger than the value obtained from equation (40).

In the following paragraphs, we investigate the effect of turbulence on the development of orientation distribution function. This is done by comparing a_{1111} with a_{1111} for Stokes flow evaluated by equations (14), (17) and (31) (denoted by $a_{1111,s}$). The orientation distribution measured at $C = 1.1$ is used as the initial condition for evaluation of $a_{1111,s}$. Each measured ϕ_o at $C = 1.1$ is used in equation (31) to evaluate ϕ at any desired downstream position. This calculation is repeated for all measured fibres and then the distribution function according to equation (14) is calculated. Finally, using equation (17), $a_{1111,s}$ for each distribution function is obtained. Considering

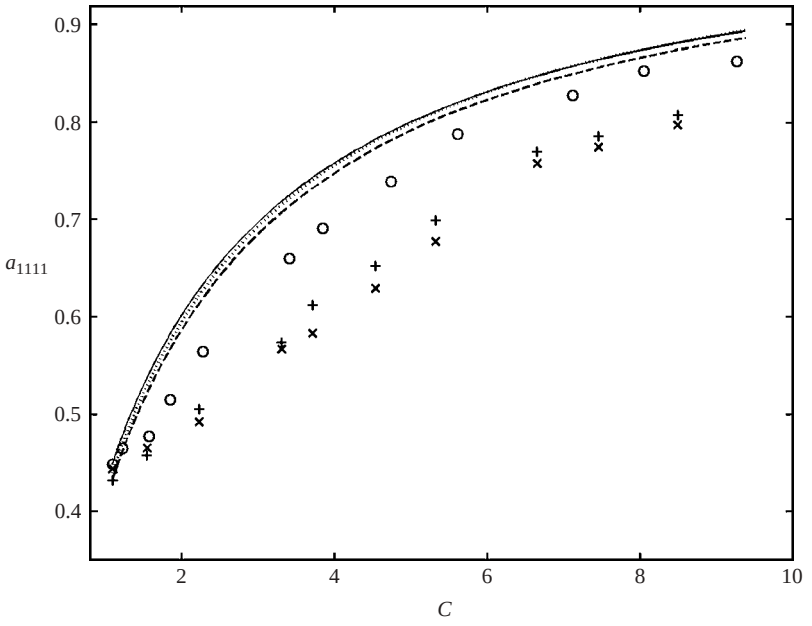

FIGURE 10. Comparison of the measured a_{1111} with the value of $a_{1111,s}$ calculated for Stokes flow ($D_r = 0$) from initial orientation distribution, ψ^p, for the three cases: $Re = 85 \times 10^3$ and $l_r = 60$; measured (○), computed (—), $Re = 85 \times 10^3$ and $l_r = 20$; measured (+), computed (- - -), $Re = 170 \times 10^3$ and $l_r = 20$; measured (×), computed (. . .).

that equation (31) is exact, the advantage of this Lagrangian approach, compared to using the Fokker–Planck equation (15), is to avoid the accumulation of the error associated with the initial distribution function of single fibres. Figure 10 shows the orientation parameter given by Stokes flow and the measured value of a_{1111}. Stokes flow overpredicts the orientation anisotropy in the contraction owing to the absence of turbulence. The small deviation between the computed orientation distribution functions by Stokes flow in figure 10 is due to unequal anisotropy of the initial profiles. The orientation distribution, ψ^p, measured downstream of the contraction inlet, at $C = 1.1$, is slightly anisotropic and differs between each case. The anisotropy in orientation distribution at this position can be attributed to the small contraction of flow in the straight channel owing to boundary-layer growth.

It is of particular interest to study the development of a_{1111} through the contraction in terms of the Reynolds number. As shown in figure 10, increasing the Reynolds number from 85×10^3 to 170×10^3 with $l_r = 20$ leads to a slight decrease in orientation anisotropy.

The effect of turbulence characteristics at the contraction inlet on orientation distribution is studied by changing the grid position relative to the contraction inlet, l_r, while keeping the Reynolds number constant at 85×10^3. At $l_r = 60$, owing to lower turbulent intensity along the contraction centreplane, a larger number of fibres align with the streamwise direction compared to $l_r = 20$. This leads to a higher value of orientation parameter in this set-up.

It is important to identify the region in the contraction where rotational diffusion has a significant influence on the dynamics of fibre orientation. Figure 11 shows the ratio of a_{1111} and evaluated orientation parameter in Stokes flow, $a_{1111,s}$, for case $Re = 85 \times 10^3$ and $l_r = 60$. The measured ψ^p at $C = 1.6$ is used as the initial

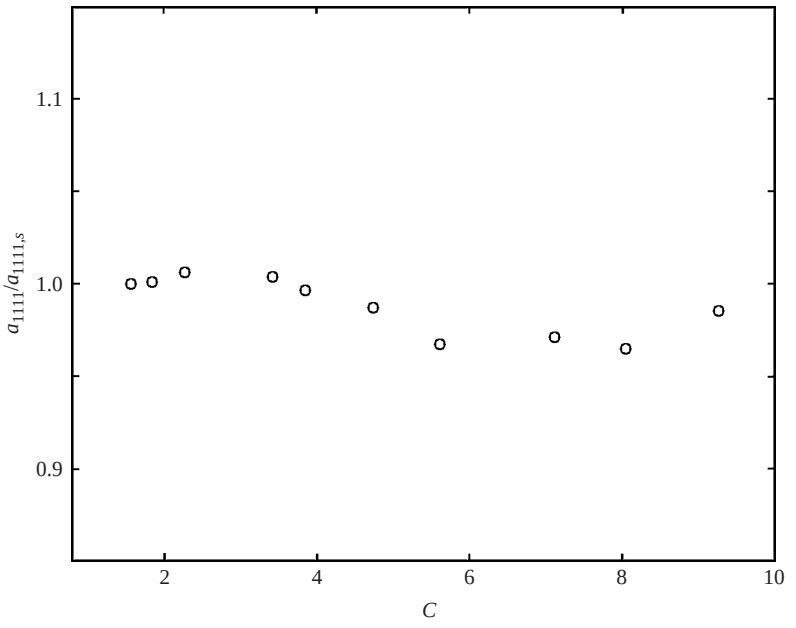

FIGURE 11. Ratio of measured and computed values of orientation anisotropy parameter based on measured ψ^p at $C = 1.6$ for $Re = 85 \times 10^3$ and $l_r = 60$.

profile for Stokes flow evaluation. As seen from this figure, the orientation parameter, a_{1111}, nearly follows the Stokes flow development at $C > 2$. To show the actual comparison of the orientation distribution functions, the normalized polar diagram of the measured and computed distribution functions at $C = 3.4$ and $C = 5.6$ are presented in figures 12 and 13, respectively. The two plots almost overlap, confirming the conclusion from figure 11. Similarly, the orientation distribution function at $Re = 85 \times 10^3$ and $Re = 170 \times 10^3$ for $l_r = 20$ follow the Stokes flow development at $C > 4$, as shown in figure 14. Comparison of the results in figures 11 and 14 shows that for the case when $l_r = 60$, the randomizing effect of turbulence becomes insignificant further upstream (i.e. lower contraction ratio) owing to the relatively lower turbulent intensity at the inlet. The fact that the orientation anisotropy at large C closely follows the prediction based on Stokes flow implies that the fibre inertia is negligible. Thus, we conclude that the microscopic Reynolds number based on fibre diameter, not the fibre length, is a more appropriate scale for the fibre dynamics. This agrees with the assumption of Bernstein & Shapiro (1994).

For all cases investigated, relative importance of turbulence disappears when the streamwise turbulence intensity falls below 1.5 %, according to figures 11 and 14. However, Pe_r is a better measure of the relative importance of turbulence and mean velocity gradient (Krushkal & Gallily 1988). Figure 15 shows the computed Pe_r based on equation (40) along the contraction centreline for all cases. Based on figures 11, 14 and 15, we conclude that the effect of turbulence on the orientation distribution function becomes insignificant when $Pe_r > 10$.

5. Discussion and conclusion

We have directly observed the influence of turbulence on the development of the orientation distribution of a dilute suspension of stiff fibres at high Reynolds number

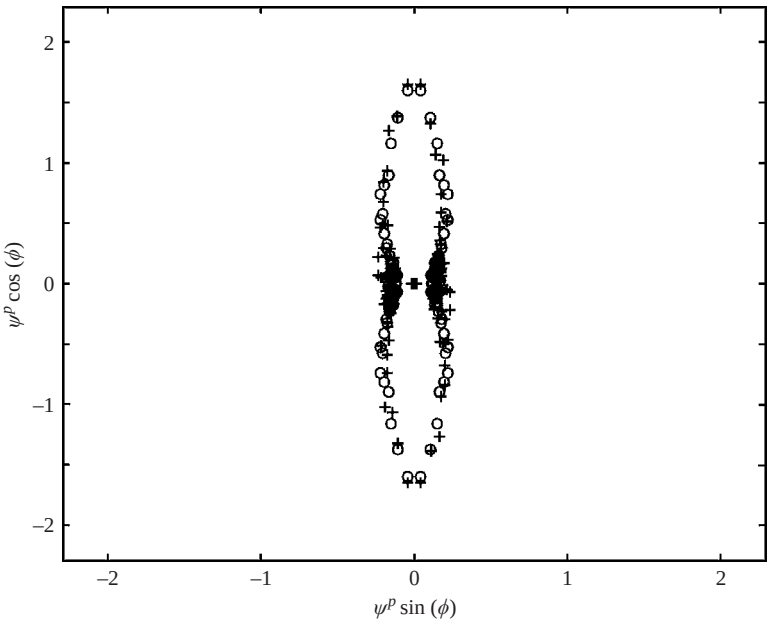

FIGURE 12. Measured (○) and computed (+) normalized orientation distribution function at $C = 3.4$, $Re = 85 \times 10^3$ and $l_r = 60$.

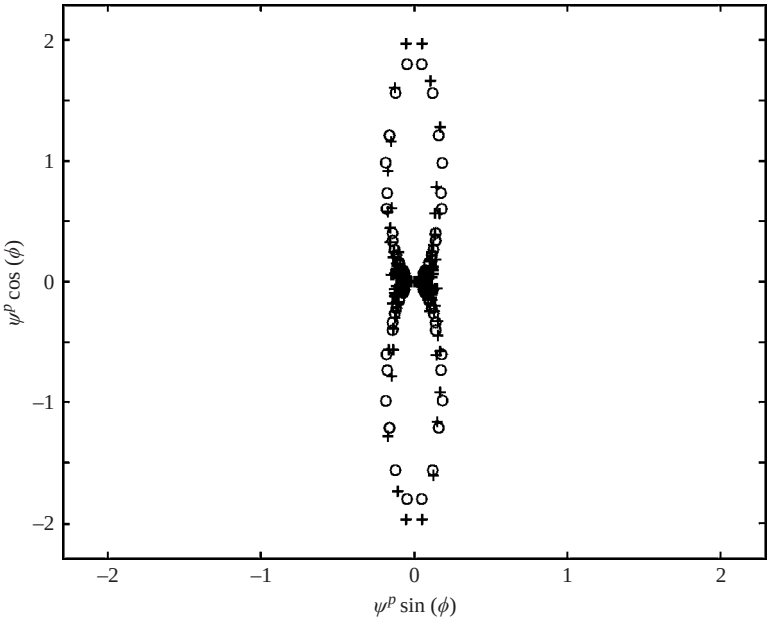

FIGURE 13. Measured (○) and computed (+) normalized distribution functions at $C = 5.6$, $Re = 85 \times 10^3$ and $l_r = 60$.

in a planar contraction. The development of orientation anisotropy at high Re flow is shown to be accurately modelled by a Fokker–Planck type equation.

Nearly isotropic homogeneous turbulence with uniform mean velocity profile is introduced at the contraction inlet. The downstream development of orientation

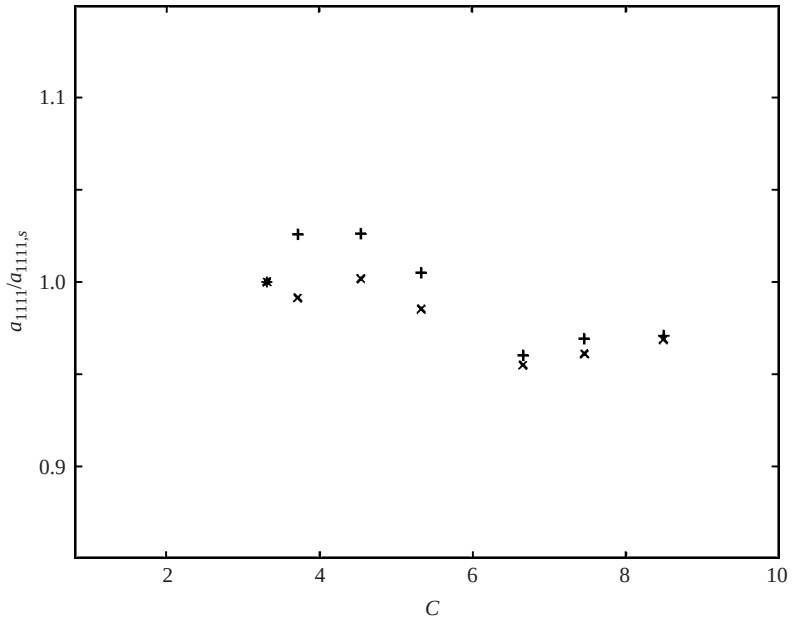

FIGURE 14. Ratio of measured and computed values of orientation anisotropy parameter based on the measured ψ^p at $C = 3.3$ for $Re = 85 \times 10^3$ and $l_r = 20$ (+), $Re = 170 \times 10^3$ and $l_r = 20$ (×).

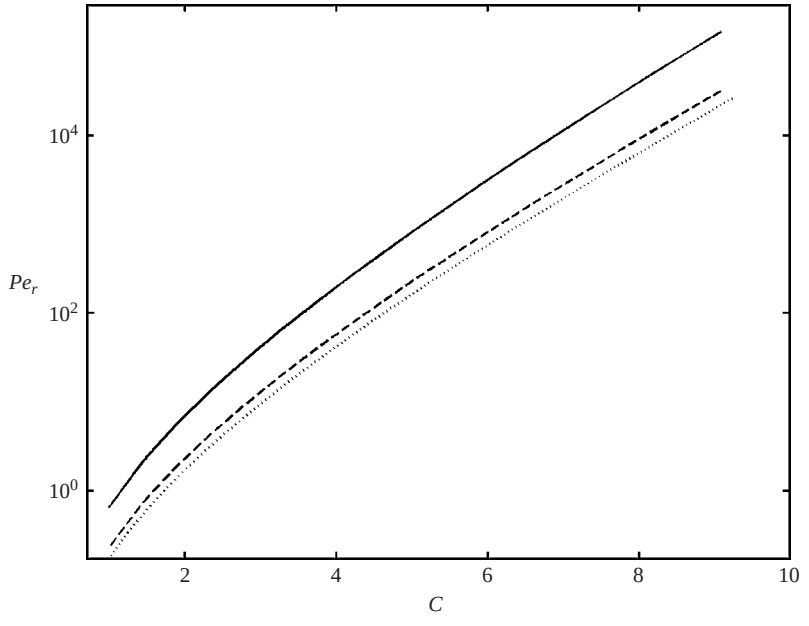

FIGURE 15. Development of Pe_r in the contraction for cases $Re = 85 \times 10^3$ and $l_r = 60$ (—); $Re = 85 \times 10^3$ and $l_r = 20$ (- - -); and $Re = 170 \times 10^3$ and $l_r = 20$ (. . .).

distribution shows that the rotational diffusion coefficient decays exponentially with local contraction ratio, C, and is dependent on inlet turbulent characteristics. However, the effect of turbulent energy production on fibre orientation in the contraction is observed to be negligible. This is attributed to the small production of turbulent energy

at $C < 2$, where turbulence closely follows the decay of grid-generated turbulence in a rectangular channel, and the large streamwise rate of strain at large C which dominates fibre orientation and offsets the effect of turbulence. In addition, the development of the orientation distribution function implies a rather weak dependence on Reynolds number. Furthermore, the results show that the influence of turbulence on fibre rotation is negligible for $Pe_r > 10$.

Since the orientation distribution function at large C develops closely to the prediction based on Stokes flow, this implies that the effect of fibre inertia is negligible. Based on the results of this work, fibre diameter is the appropriate length scale to determine the fibre Reynolds number and thus the effect of inertia.

The results obtained in this study are based on homogeneous isotropic turbulent flow with uniform mean velocity profile and negligible turbulent production at inlet. We hypothesize that the results and the empirical relation for Pe_r presented in this study may apply, in general, to planar contractions with any inlet flow conditions except in the region where production of turbulent kinetic energy may be significant.

This work was supported in part by funding from the U.S. Department of Energy under grant DE-FC36-99GO 10416. We also acknowledge assistance from Mr Paul McKay, Mr Katsumasa Ono and Dr Chang Park.

REFERENCES

Advani, S. & Tucker, C. 1987 The use of tensors to describe and predict fibre orientation in short fibre composites. *J. Rheol.* **31**, 751.

Advani, S. & Tucker, C. 1990 A numerical simulation of short fiber orientation in compression molding. *Polymer Composites* **30** *C* (10), 164.

Azaiez, J., Guenette, R. & Ait-Kadi, A. 1997 Investigation of the abrupt contraction flow of fiber suspensions in polymeric fluids. *J. Non-Newtonian Fluid Mech.* **73**, 289.

Batchelor, G. 1971 The stress generated in a non-dilute suspension of elongated particles by pure straining motion. *J. Fluid Mech.* **46**, 813.

Batchelor, G. & Proudman, I. 1954 The effect of rapid distortion of a fluid in turbulent motion. *Q. J. Mech. Appl. Maths* **7**, 83.

Becker, L. E. & Shelley, M. J. 2001 Instability of elastic filaments in shear flow yields first-normal-stress differences. *Phys. Rev. Lett.* **87**, 198301.

Bernstein, O. & Shapiro, M. 1994 Direct determination of the orientation distribution function of cylindrical particles immersed in laminar and turbulent flow. *J. Aerosol Sci.* **25**, 113.

Brenner, H. 1974 Rheology of a dilute suspension of axisymmetric Brownian particles. *Intl J. Multiphase Flow* **1**, 195.

Bunner, B. & Tryggvason, G. 1999 Direct numerical simulations of three-dimensional bubbly flows. *Phys. Fluids* **11**, 1967.

Chiba, K., Yasuda, K. & Nakamura, K. 2001 Numerical solution of fiber suspension flow through a parallel plate channel by coupling flow field with fiber orientation distribution. *J. Non-Newtonian Fluid Mech.* **99**, 145.

Cox, R. G. 1970 The motion of long slender bodies in a viscous fluid. Part 1. General theory. *J. Fluid Mech.* **44**, 791.

Dinh, S. M. & Armstrong, R. C. 1984 A rheological equation of state for semiconcentrated fibre suspensions. *J. Rheol.* **28**, 207.

Doi, M. & Edwards, S. F. 1978 *J. Chem. Soc. Faraday Trans. II.* **74**, 918.

Doi, M. & Edwards, S. F. 1988 *Theory of Polymer Dynamics.* Oxford University Press.

Goldsmith, H. L. & Mason, S. G. 1967 The microrheology of dispersions. In *Rheology: Theory and Applications*, vol. (ed. F. R. Eirich). Academic.

Goldstein, M. & Durbin, P. 1980 The effect of finite turbulence spatial scale on the amplification of turbulence by a contracting stream. *J. Fluid Mech.* **98**, 473.

Groth, J. & Johansson, A. V. 1988 Turbulence reductions by screen. *J. Fluid Mech.* **197**, 139.

Harris, J. B. & Pittman, J. F. T. 1976 Alignment of slender rod-like particles in suspension using converging flow. *Trans. Instn Chem. Engrs* **54**, 73.

Hinze, J. 1975 *Turbulence*. McGraw-Hill.

Hussain, A. K. & Ramjee, V. 1976 Effects of the axisymmetric contraction shape on incompressible turbulent flow. *J. Fluids Engng* **98**, 897.

Jeffery, G. 1922 The motion of ellipsoidal particles immersed in viscous fluid. *Proc. R. Soc. Lond.* A **102**, 161.

Koch, D. L. 1995 A model for orientational diffusion in fiber suspensions. *Phys. Fluids* **7**, 2086.

Koch, D. & Hill, R. 2001 Inertial effects in suspension and porous-media flows. *Annu. Rev. Fluid Mech.* **33**, 619.

Krushkal, E. & Gallily, I. 1988 On the orientation distribution function of non-spherical aerosol particles in a general shear flow- ii. The turbulent case. *J. Aerosol Sci.* **19**, 197.

Kwak, D., Reynolds, W. C. & Ferziger, J. H. 1975 Three dimensional time dependent computation of turbulent flows. Stanford University Rep. TF-5, Department of Mechanical Engineering, Stanford University, Stanford, CA.

Lee, M. J. & Reynolds, W. C. 1985 Numerical experiments on the structure of homogeneous turbulence. Dept. Mech. Engng Rep. TF-24, Stanford University, Stanford, CA.

Olson, J. A. 2001 The motion of fibres in turbulent flow, stochastic simulation of isotropic homogeneous turbulence. *Intl J. Multiphase Flow* **27**, 2083.

Olson, J. A., Frigaard, I., Candice, C. & Hamalainen, J. P. 2004 Modelling a turbulent fibre suspension flowing in a planar contraction: the one-dimensional headbox. *Intl J. Multiphase Flow* **30**, 51.

Olson, J. A. & Kerekes, R. J. 1998 The motion of fibres in turbulent flow. *J. Fluid Mech.* **377**, 47.

Parsheh, M. 2001 Flow in contractions with application to headboxes. TRITA-PMT Rep. 2000:16, PhD thesis, Royal Institute of Technology, Stockholm.

Prandtl, L. 1933 Attaining steady air stream in wind tunnels. *NACA Rep.* 726.

Ribner, H. & Tucker, M. 1953 Spectrum of turbulence in a contracting stream. *NACA Rep.* 1113.

Roach, P. 1987 The generation of nearly isotropic turbulence by means of grids. *Heat Fluid Flow* **8**, 82.

Taylor, G. I. 1935 Turbulence in a contracting stream. *Z. Angew Math. Mech.* **15**, 91.

Townsend, A. 1954 The uniform distortion of uniform turbulence. *Q. J. Mech. Appl. Maths* **7**, 104.

Tsuge, S. 1984 Effect of flow contraction on evolution of turbulence. *Phys. Fluids* **27**, 1948.

Tucker, H. J. & Reynolds, A. J. 1968 The distortion of turbulence by irrotational plane strain. *J. Fluid Mech.* **32**, 567.

Uberoi, M. 1956 Effect of wind-tunnel contraction on free-stream turbulence. *J. Aerosol Sci.* **23**, 756.

Ullmar, M. 1998 On fiber orientation mechanism in a headbox nozzle. TRITA-PMT Rep. 1998:8, Licentiate thesis, Royal Institute of Technology, Stockholm.

Ullmar, M. & Norman, B. 1997 Observation of fiber orientation in a headbox nozzle at low consistency. In *TAPPI Proc. Engineering and Papermakers Conf. Anaheim*, p. 865.

Westin, K. J. A., Boiko, A. V., Klingmann, B. G. B. & Alfredsson, P. H. 1994 Experiments in a boundary layer subjected to free stream turbulence. Part 1. Boundary layer structure and receptivity. *J. Fluid Mech.* **281**, 193.

Zhang, X. 2001 Fibre orientation in a headbox. Master's thesis, Mechanical Engineering Department, The University of British Columbia.